Mechanical properties of 304L stainless steel SMAW joints under dynamic impact loading

WOEI-SHYAN LEE, FAN-TZUNG TZENG
Department of Mechanical Engineering, National Cheng Kung University, Tainan 701, Taiwan, ROC
E-mail: wslee@mail.ncku.edu.tw

CHI-FENG LIN
National Center for High-Performance Computing, Hsin-Shi Tainan County 744, Taiwan, ROC

The impact properties of 304L Stainless Steel Shielded Metal Arc Welded (SMAW) joints are studied at strain rates between 10^{-3} and 7.5×10^3 s^{-1} using a compressive split-Hopkinson bar. The effects of strain rate on the flow response and fracture characteristics are fully evaluated. The results show that the tested weldments exhibit a pronounced strain rate sensitivity, and that changes in the strain rate result in a difference in the flow stress, fracture strain, and work hardening rate. Furthermore, it is noted that the strain rate sensitivity and activation volume vary with the magnitude of the strain rate, and are related to different work hardening stress levels. At all values of strain rate, the tested weldments fail as a result of adiabatic shearing, in which cracks initiate within the shear band and then propagate along this shear band until failure occurs. Observation of the fractured specimens reveals that the fracture surfaces of the fusion zone and base metal regions are characterized by the presence of elongated dimples. The variation in the observed dimple features with strain rate is consistent with the results of the impact stress-strain curves. © *2005 Springer Science + Business Media, Inc.*

1. Introduction
Type 304L stainless steel is an attractive engineering material because of its outstanding properties. It is widely used as structural steel parts in chemical, mechanical, automotive and nuclear applications. The joining of these parts is often achieved by welding, and consequently, the favorable welding characteristics of 304L SS play an important role in its selection as the material of choice. It is recognized that 304L SS can be successfully welded using a variety of techniques, including Shielded Metal Arc Welding (SMAW), Gas Tungsten Arc Welding, Submerged Arc Welding, and Plasma Arc Welding [1–4]. In their operating environments, these welded components are often required to withstand a high rate of deformation. However, the microstructure and stress state characteristics of the welded joints differ from those of the base material, and the performance of the welded structure is usually limited by the initiation of failure within the Heat Affected Zone (HAZ) of the base material, particularly within the coarse-grained region of the HAZ adjacent to the weld metal. Therefore, to ensure the reliability of large-scale structures which will be subjected to dynamic impact loading conditions, it is essential to evaluate the mechanical properties of their structural

materials, including their weld metals, under realistic operating conditions.

Actually, the mechanical behavior of various structural materials under high strain rate impact loading conditions has been studied extensively by means of the split-Hopkinson bar or a variety of alternative shock loading apparatus [5–7]. These studies have revealed that the strain rate has some degree of influence on the impact properties of most materials. Although the dynamic impact properties and associated microstructures of austenitic stainless steel have been well documented [7, 8–10], little work has been reported with regard to the impact behavior and fracture characteristics of austenitic stainless steel welded joints. Thus, the purpose of this study is to examine the impact behavior of 304L SS SMAW joints when subjected to compressive strain rates in the range of 10^{-3} to 7.5×10^3 s^{-1}. The corresponding fracture evolutions in the fusion zone and base material regions are also investigated, and are correlated with the observed impact characteristics.
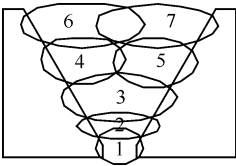
2. Experimental procedure
The base metal used in the present study was 304L stainless steel purchased from Eastern Steel Corp. (Spring

TABLE I Chemical compositions of base metal and filler metal (wt.%)

Type	Wt.%								
	C	Mn	Si	P	S	Cu	Ni	Cr	Mo
SUS304L	0.02	1.74	0.47	0.027	0.005	–	8.09	18.28	–
Filler metal (TS-308L)	0.023	1.17	0.51	0.024	0.003	0.17	9.8	20.12	0.16

TABLE II Welding parameters for Shielded Metal Arc Welding process

Multipass schematic	No. of Passes	Filler metal diameter (mm)	Current (A)	Voltage (V)	Welding speed (mm/s)	Heat input (KJ/mm^{-1})
	1	ϕ3.2	80	32.5	2.94	0.90
	2	ϕ4.0	120	30.0	2.50	1.44
	3	ϕ5.0	155	30.0	2.00	2.33
	4	ϕ5.0	155	30.0	3.49	1.33
	5	ψ5.0	150	30.0	3.06	1.47
	6	ϕ5.0	150	30.0	3.57	1.26
	7	ϕ5.0	150	30.0	2.88	1.56

House, PA) in plate form. Upon delivery, the plates were annealed at 1050°C for 1 h and then allowed to cool in air in order to remove any residual stress and to ensure a uniform microstructure. Welding of the test plates was performed using a TS-308L filler metal. This metal was supplied in the form of a spooled wire, and conformed to AWS A5.4-92 E308L-16. Note that the chemical compositions of the base material and the filler metal are provided in Table I for reference purposes. Test plates measuring $150^l \times 75^w \times 12^t$ mm^3 were machined from the annealed 304L stainless steel plates and were then butt-welded using the manual Shielded Metal Arc Welding (SMAW) process with a total of 7 welding passes. The corresponding welding parameter details are given in Table II.

Each weldment consisted of two test plates arranged such that they were welded together with a 3.2 mm root opening gap and a 1 mm root face. Prior to welding, the opposing edges of the two test plates were beveled such that they formed a single V-shaped groove with a 75° inclined angle. Following the welding process, cylindrical specimens measuring 10 mm in diameter by 10 mm in length were removed from the welded joint. As shown in Fig. 1, the location from which these specimens were taken was chosen such that each specimen would include material from the weld itself, the HAZ, and the original base metal. The end faces of the specimens were then lubricated with molybdenum disulphide grease to minimize friction effects during compression testing.

Quasi-static compression tests were conducted using a dynamic Material Testing System (MTS) at a strain rate of 10^{-3} s^{-1}. Subsequently, dynamic compression tests with high strain rates ranging from 1.5×10^3 to 7.5×10^3 s^{-1} were performed using a compressive split-Hopkinson bar system. Specific apparatus, data recording, experimental and calculation methodology have been described in our previous work [11]. For the optical microscopic observations of the microstructure, the specimens were first etched in a solution of 32% HNO$_3$, 32% HCl, and 36% H$_2$O (by volume) for 1 minute, and then examined through a Reichert Jung MeF3 optical microscope. Following specimen failure,
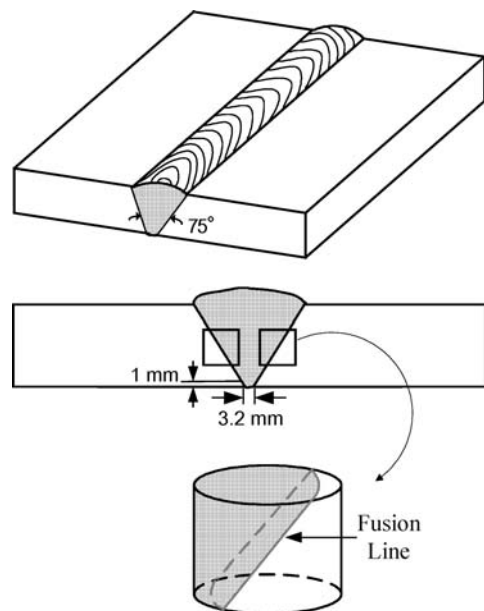

Figure 1 Schematic representation of specimens used in SMAW welding.

the fracture features of specimens were examined by means of a Jeol JXA 840 SEM operating at an acceleration potential of 15 kV.

3. Results and discussion
### 3.1. Microstructures of undeformed weldment

Fig. 2a presents an optical micrograph of the base metal, Heat Affected Zone (HAZ), and fusion zone of an undeformed 304L SS GTAW weldment. The base metal consists of ferrite phases (dark) with a volume of approximately 2%, and polygonal austenite grains (light), while the fusion zone contains δ-ferrite formations with a volume of 11%, characterized by a columnar dendritic structure. Epitaxial growth of the grains in the fusion zone from the grains of the base metal is observed along the direction of the maximum temperature gradient. Fig. 2b shows the microstructure of the uppermost welding pass of the fusion zone, in which the δ-ferrite is shown as columnar dendrite. The micrograph
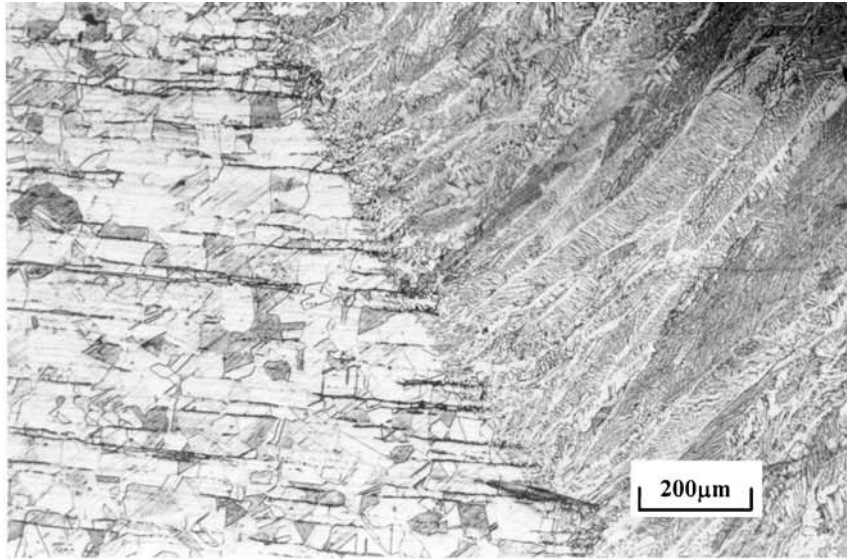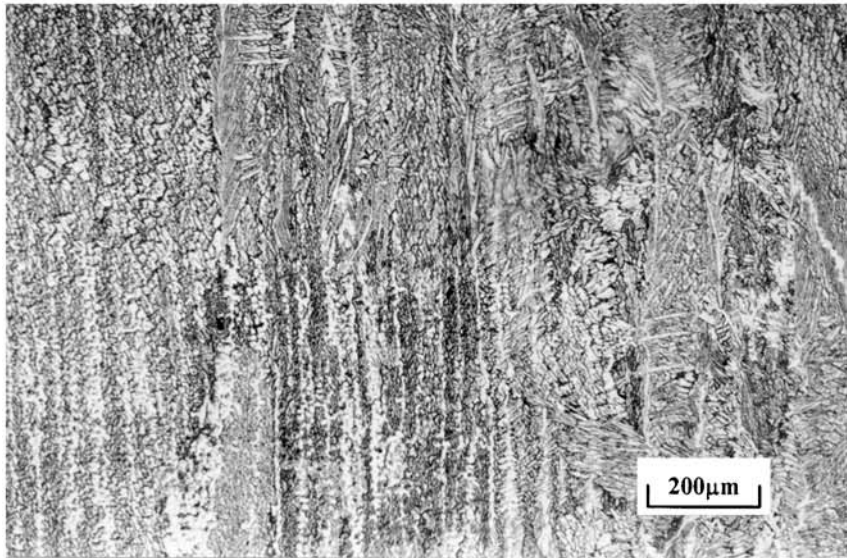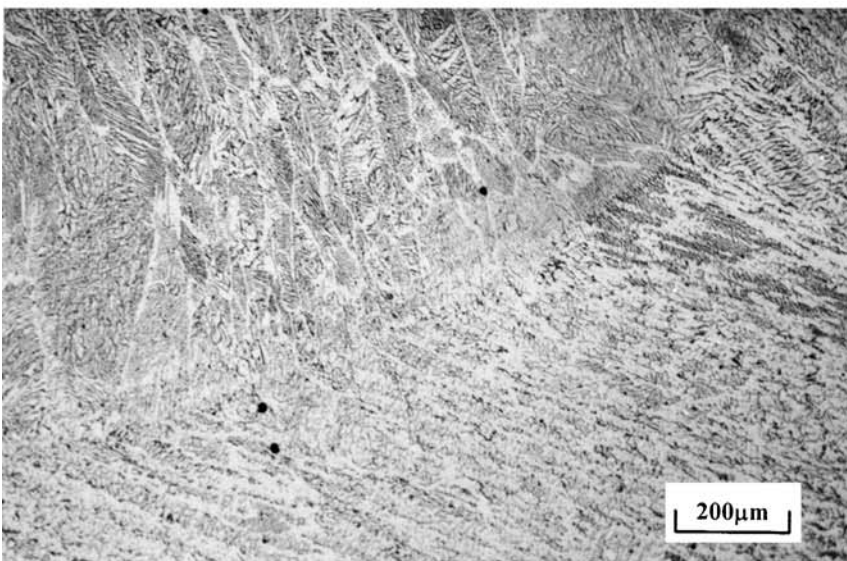
Figure 2 Optical micrographs of 304L SS SMAW weldment at (a) interface of base metal and fusion zone; (b) top pass of fusion zone; (c) at the interface between 4th and 5th passes of fusion zone.

presented in Fig. 2c shows the interface between the 4th and 5th welding passes at a location in the middle of the fusion zone. The general feature of the presented microstructure is that of a wide variation in the ferrite morphology within the fusion zone, which arises from the adopted multi-pass welding process. A comparison of Figs 2b and c indicates that the microstructures in the fusion zone are extremely heterogeneous, i.e. the ferrite morphology changes from a columnar dendrite arrangement in the uppermost welding pass to a vermicular formation in Fig. 2c. This phenomenon is the result of the thermal cycle associated with each welding pass. The weld cooling rate varies from pass to pass, and accordingly, the fraction of ferrite transformation and morphology within each welding pass differs.

3.2. Stress-strain response

Fig. 3a presents typical true stress-true strain curves of the 304L SS SMAW weldment for different strain rates in the range of 10^{-3} to 7.5×10^3 s^{-1}. At each strain rate, results from three tests are presented. For each curve, the weldment exhibits a work hardening effect in the initial stages of deformation. Subsequently, the
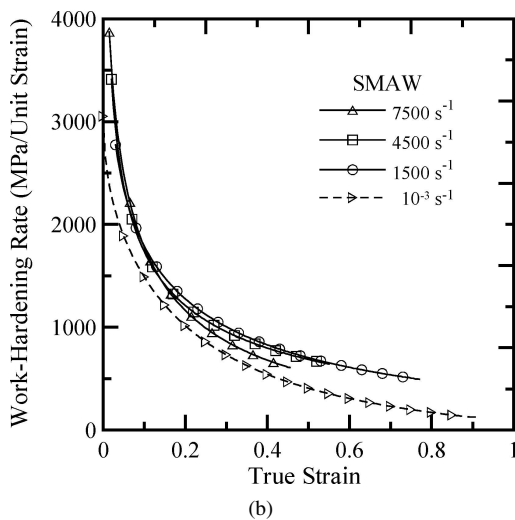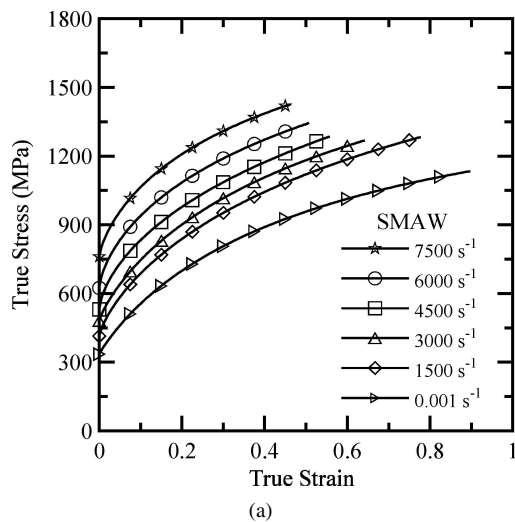
TABLE III Yielding strength (σ_y), Material constant (B), and work hardening coefficient (n) of 304L SS SMAW weldment deformed at different strain rates

Strain rate (s^{-1})	σ_y (MPa)	B (material constant)	n (work hardening coefficient)	ε_f (fracture strain)
0.001	335.0	1035	0.70	0.90
1500	413.7	1102	0.66	0.78
3000	480.5	1038	0.63	0.64
4500	530.3	1060	0.62	0.55
6000	624.3	1046	0.59	0.50
7500	761.0	1016	0.58	0.46

flow stress attains a peak value, at which fracture of the weldment occurs. A comparison of the curves presented in Fig. 3a shows that the 304L SS SMAW weldment is sensitive to the strain rate, i.e. an increased flow stress is developed when deformation takes place at an increased strain rate. Moreover, in the dynamic loading regime, there is an increase in this rate sensitivity as the strain rate increases. It is also of interest here to examine the effect of the strain rate on the fracture
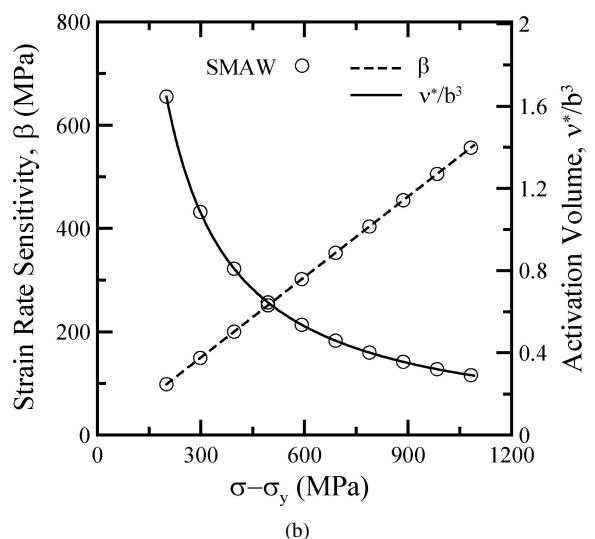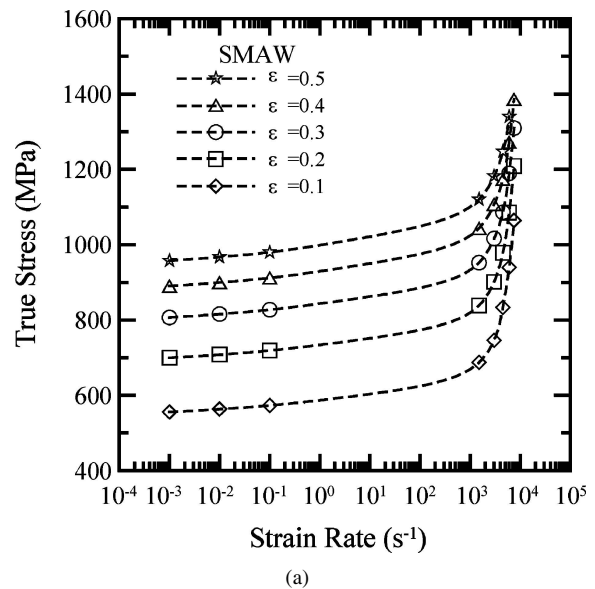

(a)

(b)

Figure 3 (a) Typical flow stress-strain curves of 304L SS SMAW weldment deformed at different strain rates ranging from 10^{-3} to 7.5×10^3 s^{-1}; (b) Variation in work hardening rate as a function of strain and strain rate.

(a)

(b)

Figure 4 (a) Influence of strain rate on flow stress under different plastic strains; (b) strain rate sensitivity and activation volume as a function of work hardening stress.

strain. An inspection of the results presented in Fig. 3a and Table III shows that the fracture strain of a 304L SS weldment which is deformed at a high strain rate is generally lower than when the weldment is strained at a quasi-static rate, i.e. the weldments fracture at true strains of 0.9 and 0.46 under strain rates of 10^{-3} and 7.5×10^3 s^{-1}, respectively. From these results, it can be concluded that the ability of the weldment to resist fracture is degraded as the applied strain rate increases.

The results of Fig. 3a indicate that the impact response of the 304L SS SMAW weldment exhibits a greater degree of work hardening under dynamic loading conditions than when the specimens is deformed quasi-statically at a strain rate of 10^{-3} s^{-1}. The flow stress-strain relationship presented in Fig. 3a can be described by the general empirical work hardening law proposed by Ludwik [12], i.e.

$$\sigma = \sigma_y + B\varepsilon^n \tag{1}$$

where σ_y is the yield strength, B is the material constant, and n is the work hardening coefficient. Application of this law to the current measurement results gives the variations in σ_y, B and n with strain rate, as shown in Table III. In general, it can be seen that the yield strength increases with an increasing strain rate in both the quasi-static and the dynamic regimes. However, the material constant, B, and the work hardening coefficient, n, both tend to decrease as the applied strain rate increases. The decrease of material constant B with an increase of strain rate implies that the strengthening effect of tested weldment is reduced by deformation heat when high velocity impact loading condition is imposed.

As mentioned previously, the plastic flow response of the weldment is related to the magnitude of the applied strain rate, which induces different work hardening behaviors. The slopes of the stress-strain curves in Fig. 3a can be used to define the work hardening rate of the weldment at a given strain rate. A typical plot of the work hardening rate against the true strain for different values of strain rate is presented in Fig. 3b. As is to be expected, the work hardening rate is seen to decrease with an increasing strain at all values of the strain rate. It can reasonably be assumed that this is the result of microstructural changes and an increased deformation heat as the strain increases. Regarding the effect of the strain rate on the work hardening behavior, it is determined from Fig. 3b that for values of true strain less than 0.1, the work hardening rate increases slightly with increasing strain rate. Conversely, at true strain values exceeding 0.1, the work hardening rate appears to decrease as the strain rate is increased. This result can be attributed to the adiabatic deformation heat induced in the loading process.
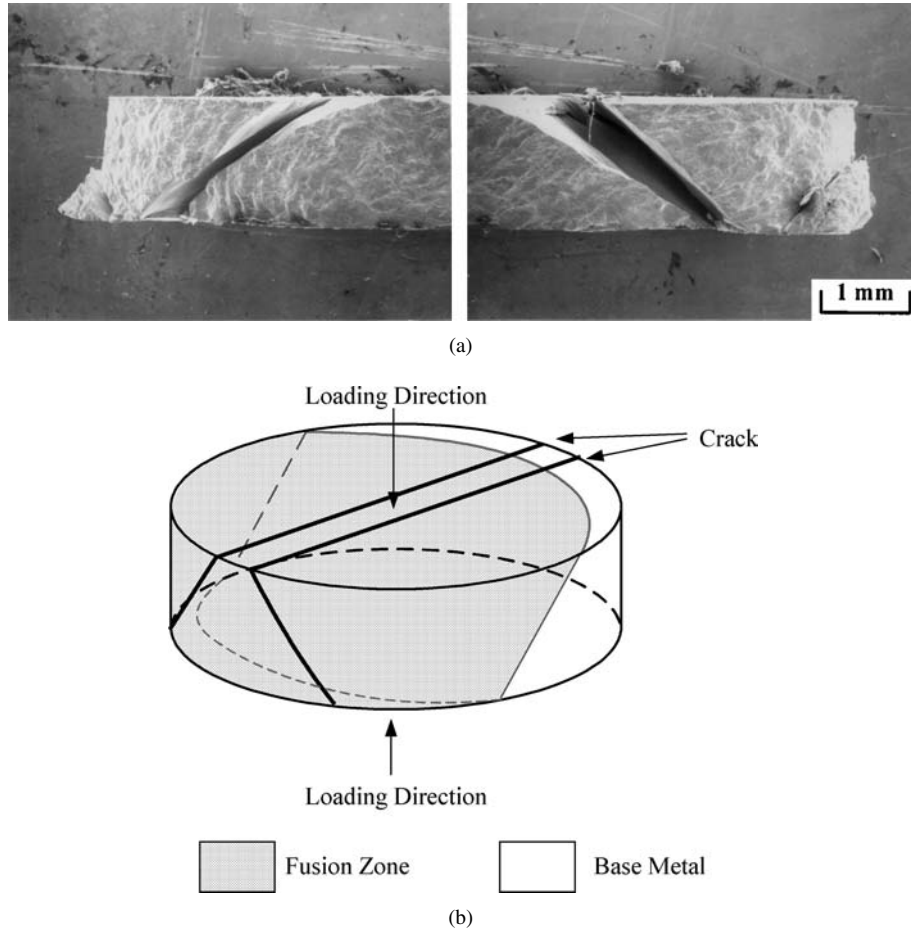

(a)

(b)

Figure 5 (a) Fractograph of tested weldment after fracture at strain rate of 4.5×10^3 s^{-1}; (b) Schematic representation of fracture features and orientation of adiabatic shear band.

### 3.3. Strain rate dependence and thermally activation volume estimation

The strain rate dependence of a material's dynamic properties is an important aspect of its constitutive relation. Although the stress-strain curves of the 304L SS SMAW weldments presented in Fig. 3a indicate that the strain rate sensitivity increases at higher values of the applied strain rate, the relationship between the strain rate sensitivity and the strain rate is easier to visualize if a semi-logarithmic plot of the flow stress at constant strain versus the strain rate is constructed. Accordingly, Fig. 4a presents the variations of the flow stress with increasing strain rate at various constant strain levels. From the results of this figure, it can be surmised that the strain rate sensitivity increases rapidly for applied strain rates of 10^3 s^{-1}, or higher. This abrupt change in the strain rate sensitivity of the flow stress is likely to be the result of the increasing influence of dislocation drag mechanisms in this region, and by the evolution of the strength/strain-rate dependence into a linear form [13]. However, some researchers have also demonstrated that the increased rate sensitivity identified in this load regime is caused by a high rate of dislocation generation, and by the rapid formation of twin structures and martensite transformation [7, 14].

The strain rate dependence of the flow stress may be determined by calculating the mean apparent strain rate sensitivity parameter, which is defined as:

$$\beta = (\sigma_2 - \sigma_1)/\ln(\dot{\varepsilon}_2/\dot{\varepsilon}_1) \qquad (2)$$

where σ_1 and σ_2 are the flow stresses measured at a given strain, ε, and temperature, T, at strain rates of $\dot{\varepsilon}_1$ and $\dot{\varepsilon}_2$, respectively. Under high strain rate deformation, the variation of the strain rate sensitivity relates to the thermal activation energy, which is a function of the local stress and the absolute temperature. The slopes of the strain rate sensitivity curves presented in Fig. 4a can be used to calculate the activation volume via the
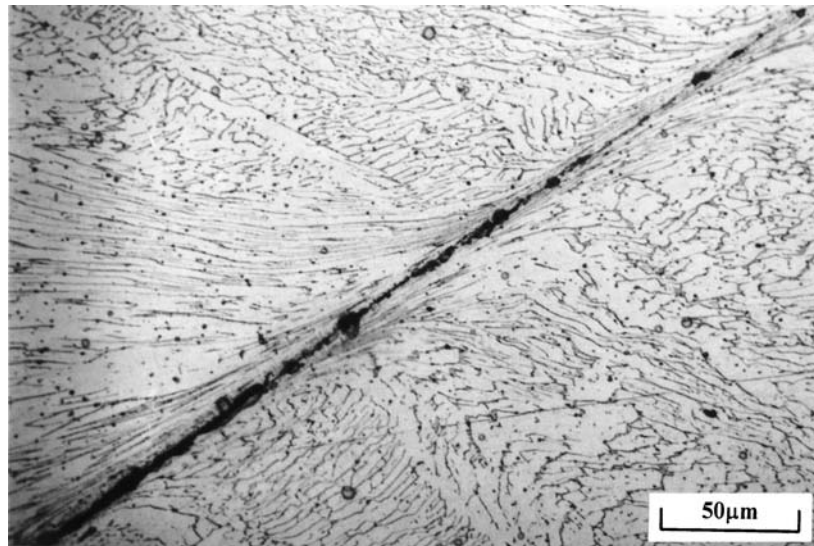
(a)
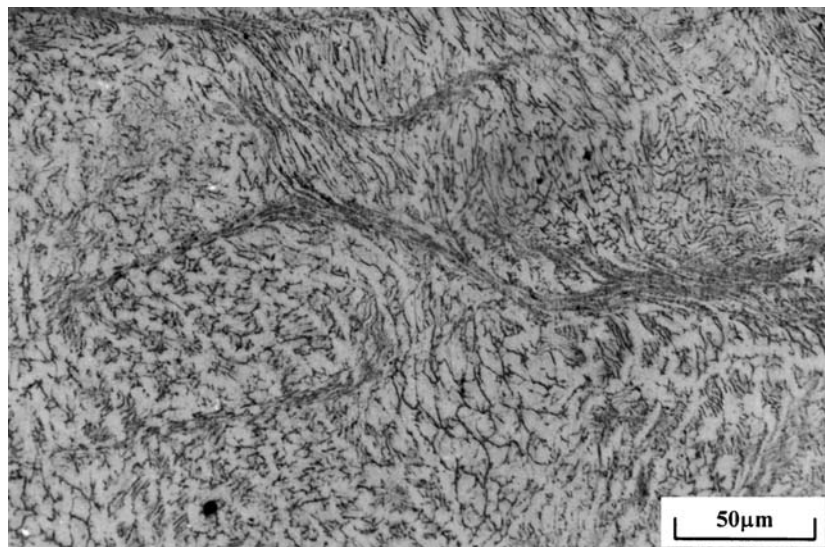
(b)

Figure 6 (a) Formation of adiabatic shear band in fusion zone deformed at 3×10^3 s^{-1}; (b) Occurrence of intensive localized unstable flow between two adiabatic shear bands.

following expression:

$$(\partial \ln \dot{\varepsilon}/\partial \sigma^*)_T = -(\partial G^*/\partial \sigma^*)/KT = v^*/KT \quad (3)$$

where $\sigma^* = \sigma - \sigma_i$ (σ_i is the long-range internal stress caused by other dislocations or by the back stress arising from curvature of the slip dislocations), and v^* is the activation volume. Ezz and Hirsoh [15] associated σ_i with σ_y, and σ^* with σ_h. Here σ_h is the working-hardening contribution, which is a function of plastic strain, strain rate, and temperature. Since strain rate sensitivity $\beta = KT/v^*$ and $v^* \propto 1/\sigma^*$, as $\sigma^* \sim (\sigma - \sigma_y)$, the v^* value can be plotted as a function of $\sigma - \sigma_y$, that is, $v^* \propto 1/(\sigma - \sigma_y)$. Based the data plotted in Fig. 4a, the calculated value of v^* normalized with respect to b^3 (for 304L stainless steel, the Burgers vector $b = 2.64$ Å) plotted in Fig. 4b shows that the decrease of v^* correlates with increasing work-hardening stress for 304L SS SMAW weldment. The small work-hardening stress corresponding to the characteristic rapid increase

in activation volume implies that thermal activation energy reduce the stress required to force a dislocation past an obstacle during deformation. With regard to the strain rate sensitivity, a linear relationship between strain-rate sensitivity and work-hardening stress is observed for 304L SS SMAW weldment. This implies that the increasing strain rate sensitivity noted with increasing work-hardening stress is caused by the evolution of different microstructures and by different degrees of work-hardening. The significant contribution to the work-hardening capacity is believed to arise from the presence of a number of dislocations during deformation.

3.4. Observations of fracture characteristics

Fractographic examination of the impacted weldments reveals that adiabatic shearing is the primary fracture mechanism. Under each of the dynamic testing conditions considered in the present investigation, the
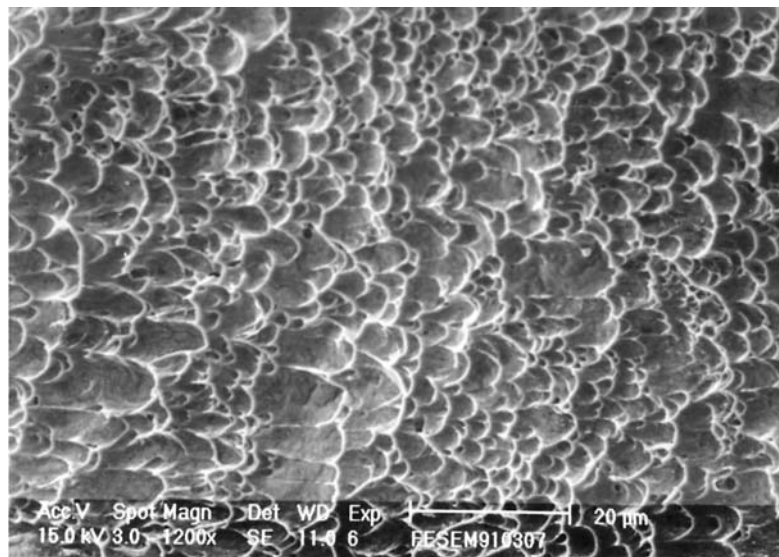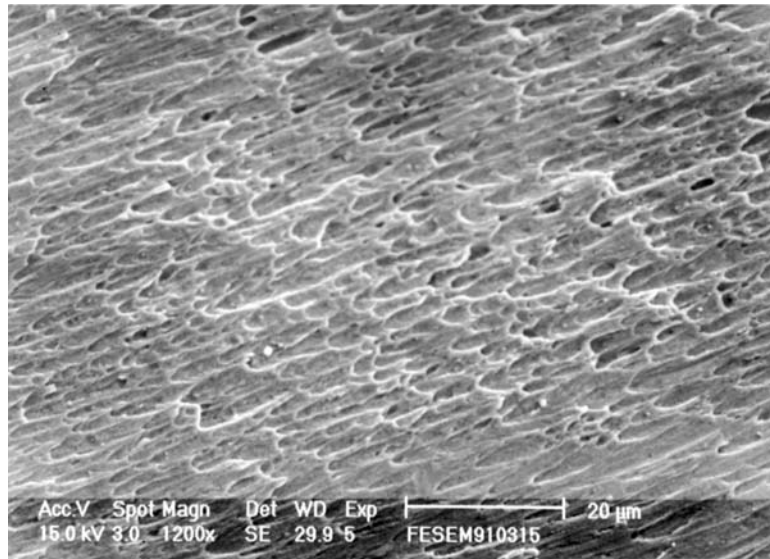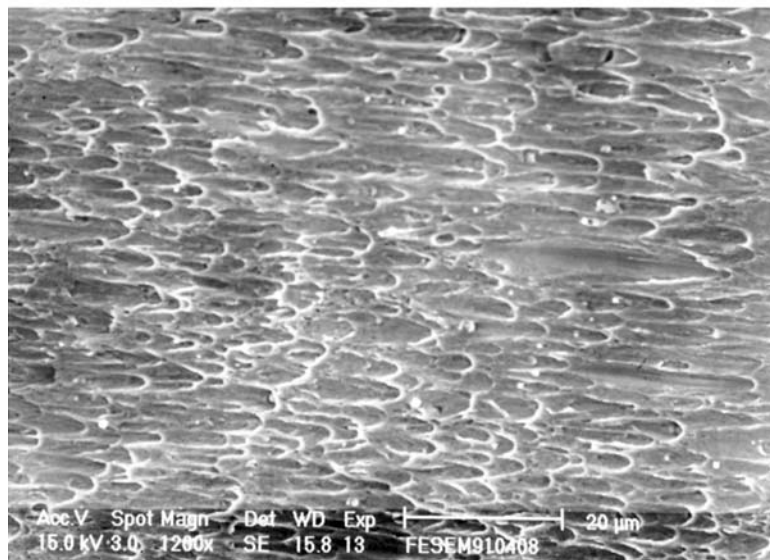

(a)
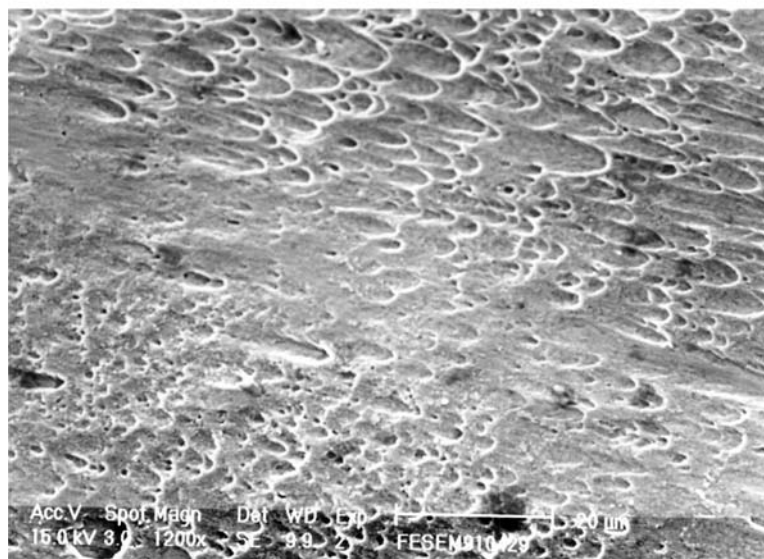
(b)

Figure 7 Fracture feature of base metal and fusion zone deformed at two different strain rates: (a) base metal, $\dot{\varepsilon} = 1.5 \times 10^3$ s^{-1}; (b) base metal, $\dot{\varepsilon} = 7.5 \times 10^3$ s^{-1}; (c) fusion zone, $\dot{\varepsilon} = 1.5 \times 10^3$ s^{-1}; (d) fusion zone, $\dot{\varepsilon} = 7.5 \times 10^3$ s^{-1}. *(Continued on next page).*

(c)

(b)

Figure 7 (*Continued*).

weldments failed in a catastrophic manner along planes inclined at 40–50° to the direction of impact (i.e. along the plane of maximum shear stress). Fig. 5a shows a low magnification side view micrograph of the weldment after fracture under an applied strain rate of 4.5×10^3 s^{-1}. It can be seen that cracking along the adiabatic shear band has resulted in a separation of the specimen. Under high velocity impact loading, it is known that the plastic work associated with the deformation generates a temperature rise within the specimen and a corresponding change in the microstructure. The rate by which the temperature increases depends upon the heat produced by the deformation and upon the thermal conductivity of the material, i.e. if the rate at which heat is produced is greater than the rate at which it is conducted away from the region of deformation, the local temperature will increase, and an adiabatic shear band will be formed. Fig. 5b presents a schematic illustration of the observed fracture surface features, and reveals that the adiabatic shear band extends across both the fusion zone and the base metal

regions. Furthermore, it is noted that fracturing does not take place at the interface of the base metal and fusion zone regions, which demonstrates that the tested weldment possesses favorable weldability characteristics, i.e. the interfacial strength in the vicinity of the fusion line is higher than that in either the fusion zone or the base metal region. Fig. 6a shows the formation of adiabatic shear bands in the fusion zone regions in a weldment deformed at 3.0×10^3 s^{-1}. Localized plastic flow is evident in the shear deformation zone, and the presence of well-developed cracks is noted within the shear bands. Fig. 6b shows the top surface of the cylindrical specimen. The microstructure of the region between two adiabatic bands is characterized by intensive localized strain variations and by inhomogeneous deformation.

Although the observed fracture features of the base metal and fusion zone regions both depend strongly on the applied strain rate, a comparison of the two fracture surfaces reveals certain differences in the evolution of the fracture features. Figs 7a and b show the fracture

4846

features of the base metal when deformed at strain rates of 1.5×10^3 and 7.5×10^3 s^{-1}, respectively. In both cases, the fracture surfaces contain dimples which exhibit pronounced elongation along the shear direction. The presence of these dimple structures indicates that the base metal has failed in a ductile manner. However, a comparison of the two figures shows that the characteristics of the two dimpled surfaces are not identical. For example, it can be seen that as the strain rate increases, the size of the elongated dimples also increases, but that the density of the dimples decreases. Furthermore, the region with a flat facet becomes more apparent at a higher strain rate. It is possible that the changes in fracture characteristics described above may cause a degradation of the weldment's fracture resistance in the base metal region. Figs 7c and d show the fracture features of the fusion zone for weldments deformed at strain rates of 1.5×10^3 and 7.5×10^3 s^{-1}, respectively. It is clear that the forms of the fusion zone fracture surfaces are different from those of the base metal, i.e. although the surfaces still contain elongated dimples, they are flatter than those observed in the base metal. A comparison of Fig. 7c with Fig. 7d shows that the fracture features are also dependent upon the magnitude of the applied strain rate, i.e. although the surface in Fig. 8d is still dimpled, some cleavage features are observed in the matrix. The formation of a dimple-like fracture surface with cleavage facets implies that the ductility and fracture resistance of the fusion zone both degrade when a high strain rate loading condition is imposed. The variations in the dimpled surfaces observed in both the base metal and the fusion zone regions as the strain rate is increased correlate well with the characteristics of the flow stress-strain curves presented previously in Fig. 3a, i.e. the fracture strain of the 304L SMAW weldment decreases as the strain rate is increased.

4. Conclusions

Effects of strain rate on the impact properties and failure behavior of 304L SS SMAW weldments have been studied. As the strain rate increases, it has been observed that the flow stress increases and that the fracture strain decreases. This result has been verified through a careful observation of the corresponding fracture features. An increased strain rate sensitivity and a decreased activation volume have been identified as the work hardening stress increases. SEM analysis of the fractured weldments has shown that the main fracture mechanism is one of adiabatic shearing, in which cracking takes place at an angle of 40–50 degrees with respect to the direction of impact. The fracture surfaces of both the fusion zone and the base metal regions are characterized by a dimpled structure, where the size and density of the dimples are dependent upon the magnitude of the applied strain rate. A relative brittle behaviour is found in the fusion zone.

References

1. O. KAMIYA and K. KUMAGAI, *J. Mater. Sci.* **25** (1990) 2017.
2. M. SIRESSHA, V. SHANKAR, SHAJU K. ALBERT and S. SUNDARESAN, *Mater. Sci. Eng.* **A292** (2000) 74.
3. G. M. REDDY, T. MOHANDAS and K. K. PAPUKUTTY, *J. Mater. Process. Technol.* **74** (1998) 27.
4. H. D. STEFFENS and H. KAYSER, *Weld. J.* **51** (1972) 408.
5. D. E. ALBERT and G. T. GRAYIII, *Acta Mater.* **45** (1997) 343.
6. K. P. STAUDHAMMER, C. E. FRANTZ, S. S. HECKER and L. E. MURR, in "Shock Waves and High Strain-Rate Phenomena in Metals," edited by M. A. Meyers and L. E. Murr (Plenum Press, New York, NY, 1981) p. 91.
7. W. S. LEE and C. F. LIN, *Metall. Mater. Trans.* A **33A** (2002) 2801.
8. S. L. SEMIATIN and J. H. HOLBROOK, *Metall. Trans.* **14A** (1983) 1681.
9. S. S. HECKER, M. G. STOUT, K. P. STAUDHAMMER and J. L. SMITH, *ibid.* **13A** (1982) 619.
10. L .E. MURR, K. P. STAUDHAMMER and S. S. HECKER, *ibid.* **13A** (1982) 627.
11. W. S. LEE and C. F. LIN, *Mater. Sci. Eng.* A **308** (2001) 124.
12. P. LUDWIK, in "Elemente der Technologischen Mechanik" (Springer, Berlin, 1909) p. 32
13. P. S. FOLLANSBEE and U. F. KOCKS, *Acta Metall.* **36** (1988) 81.
14. F. J. ZERILL and R. W. ARMSTRONG, *Acta Metall. Mater.* **40** (1992) 1803.
15. S. S. EZZ and P. B. HIRSOH, *Phil. Mag.* A **69** (1994) 105.